Original scientific paper
https://doi.org/10.33180/InfMIDEM2023.306

Informacije MIDEM
Journal of Microelectronics,
Electronic Components and Materials
Vol. 53, No. 3(2023), 191 – 202

A Comprehensive Strategy for Modelling the Conducted EMI of an Integrated Motor Drive in the Time Domain

Kristjan Saksida[1,2], Marko Jankovec[2]

[1]Pre-development Mechatronics, MAHLE Electric Drives Slovenija d.o.o., Šempeter pri Gorici, Slovenia
[2]Laboratory of Photovoltaics and Optoelectronics, Faculty of Electrical Engineering, University of Ljubljana, Ljubljana, Slovenia

Abstract: The paper introduces a comprehensive strategy for modelling the conducted electromagnetic interference (EMI) of a 48 V 11,2 kW permanent magnet motor drive with an integrated three-phase inverter in the time domain to comply with the CISPR 25 standard. The strategy is based on transient electrical simulations using LTspice® and EMI receiver modelling by signal post-processing in MATLAB®. To extract AC lumped component parameters for electrical simulations of the inverter, the Ansys® Q3D Extractor® environment was employed, while the electrical parameters of the motor side were determined from an impedance analyzer measurement. Two distinct transient simulations were performed and compared, namely a static PWM and a Space Vector Pulse Width Modulation (SVPWM) control strategy, where for the latter the simulation time was chosen to capture one electrical revolution of the motor. For the EMI receiver simulation, a digital Short-Time Fourier Transform (STFT) algorithm, compliant with CISPR 1611, was implemented. The simulation of one electrical revolution of the motor lasted 43 minutes, resulting in the average spectral deviation between the measured and simulated spectrum bandwidth of 3,33 dBµV and 2,58 dBµV for peak and average detectors, respectively. The introduced strategy proposes a straightforward approach for the extraction of parasitic elements. Furthermore, it ensures accurate EMI prediction without compromising simulation time, which is crucial to stay within the timeframe when developing an automotive product.

Keywords: EMI modelling; integrated motor drive; FFT EMI receiver; SVPWM; transient analysis

Celostni pristop k modeliranju prevodnih elektromagnetnih motenj integriranega elektromotorskega pogona v časovni domeni

Izvleček: Članek predstavlja celovito strategijo modeliranja prevodnih elektromagnetnih motenj (EMI) elektromotorskega pogona s trajnimi magneti (48 V, 11,2 kW), ki ima integriran trifazni pretvornik, v skladu s standardom CISPR 25. Strategija temelji na uporabi orodja LTspice® za analizo v časovnem prostoru in na modeliranju EMI sprejemnika s post-obdelavo signalov v okolju MATLAB®. Za pridobivanje parazitnih parametrov, ki so potrebni za električne simulacije pretvornika, je bilo uporabljeno okolje Ansys® Q3D Extractor®, medtem ko so bili električni parametri na strani motorja določeni z impedančnim analizatorjem. Izvedeni in primerjani sta bili dve različni časovni simulaciji. Prva je temeljila na statičnem PWM krmiljenju mostiča, druga pa na pulzno-širinski modulaciji v vektorskem prostoru (SVPWM), pri čemer je bilo za slednjo določeno trajanje simulacije na podlagi zajema enega električnega obrata motorja. Pri simulaciji EMI sprejemnika je bila v skladu s CISPR 16-1-1 implementirana časovno kratka Fourierjeva transformacija (STFT). Simulacija enega električnega obrata motorja je trajala 43 minut. Povprečno odstopanje med merjenim in simuliranim spektrom na frekvenčnem območju zanimanja je za detektor vršne vrednosti znašalo 3,33 dBµV, za detektor povprečne vrednosti pa 2,58 dBµV. Predstavljena strategija predlaga preprost pristop za določanje parazitnih parametrov. Poleg tega zagotavlja zadovoljivo napoved EMI, vendar ne na račun podaljšanja trajanja simulacije, kar je ključno za upoštevanje časovnih omejitev pri razvoju izdelka za avtomobilski trg.

Ključne besede: EMI modeliranje; integriran elektromotorski pogon; FFT EMI sprejemnik; SVPWM; analiza v časovnem prostoru

** Corresponding Author's e-mail: kristjan.saksida@mahle.com*

How to cite:
K. Saksida et al., "A Comprehensive Strategy for Modelling the Conducted EMI of an Integrated Motor Drive in the Time Domain", Inf. Midem-J. Microelectron. Electron. Compon. Mater., Vol. 53, No. 3(2023), pp. 191–202

1 Introduction

During the development phase of an automotive product, strict project timelines and budget limitations must be considered and not taken separately from the technical aspect. Having fewer iteration loops also means using fewer project resources.

Development of an integrated motor drive is a good example, where failing to reach electromagnetic compatibility (EMC) requirements could lead to major correction loops of the entire design. An accurate and fast electromagnetic interference (EMI) prediction is therefore crucial to stay within the project timeline and budget boundaries. To mitigate the simulation time, researchers mainly propose a frequency domain instead of a time domain approach, simply claiming that the time domain simulation takes too long to complete [1]–[3]. However, they do not reveal actual simulation times [4]–[6].

Regardless of the simulation domain, many papers focus on methodologies for the extraction of lumped parameters. Frequently, they focus intensively on a particular component of the system, such as a switching device, PCB, or motor, while oversimplifying other elements. However, they often lack support from a sensitivity study addressing the omitted parameters that influence the EMI spectrum.

In terms of modeling switching devices, authors mainly focus on adequately describing current and voltage transition slopes, recognizing these phenomena as the main source of the EMI [4], [5], [7], [8].

The determination of lumped parameters of a PCB is typically approached in two ways. One method involves analytical techniques, particularly suitable for straightforward geometries. Alternatively, for more intricate structures, such as multilayer configurations, parasitic extraction software is often employed [5].

When modelling a motor, the finite element method (FEM) yields good results; however, managing mechanically complex electrical machine geometries is a time-consuming task [9]. Based on this fact, many researchers propose a method, where a complex motor model is built from different impedance measurements [10]–[15]. Keeping the rotor position in mind, the method is suitable for induction and permanent magnet motors.

Last but not least, in many cases the EMI receiver models are either not implemented or the specifics not documented or referenced, resulting in a questionable comparison of a simulated and measurement results [1]–[6].

This paper proposes a comprehensive strategy for modelling the conducted emissions of an integrated motor drive, ensuring that spectrum accuracy is not compromised by simplifications that lead to simulation time mitigation. The paper indicates the lumped parameters with significant effect to the EMI spectrum and objectively addresses the simulation time duration, aiming to keep it below 1 hour. In conjunction with non-symmetrical parasitic elements, it also evaluates the impact of a motor control strategy implementation on the EMI spectrum. Furthermore, it indicates the minimum simulation time needed to capture all EMI phenomena of an integrated motor drive within the dwell time of the EMI receiver.

The equipment under test (EUT) was MAHLE 48 V 11,2 kW permanent magnet motor drive (see Fig. 1) with an integrated 3phase inverter that must comply with the CISPR 25: 2016 standard for Conducted and Radiated Emissions [16], [17]. The standard prescribes an EUT to operate under typical loading conditions. To simplify the test setup, the EUT was used without a load in a fixed operating point.

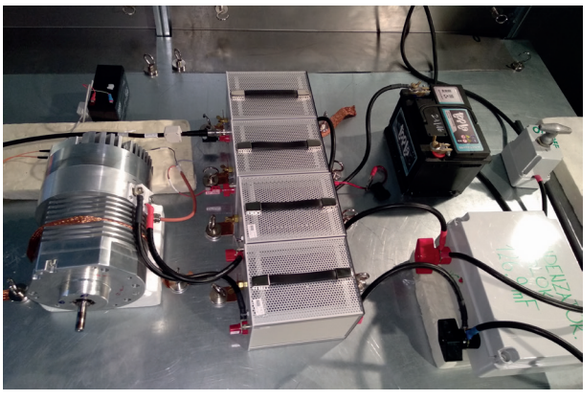

Figure 1: MAHLE 48 V 11.2 kW integrated motor drive with test setup according to CISPR 25.

2 Frequency & time domain approach

SPICE based simulators are commonly used for electronic circuits simulation. Modelling of EMI phenomena consists of modelling the EUT itself as well as the test setup specifics according to an applied standard. Many authors propose to use frequency domain approach which gives almost an instant simulation result, that is spectral density on the measurement node [1]–[3]. This approach usually gives adequate results when simulating low power motor drives where the dimensions and with that all parasitic phenomena are limited to the components themselves.

However, when the dimensions increase and with that nonsymmetrical parasitic elements are introduced, the simplification of the *di/dt* and *du/dt* transients with current and voltage sources respectively, deteriorates simulation accuracy. High power motor drives usually consist of multiple printed circuit board assemblies (PCBAs), where additional parasitic elements are introduced with interfaces between these boards (see Fig. 2).

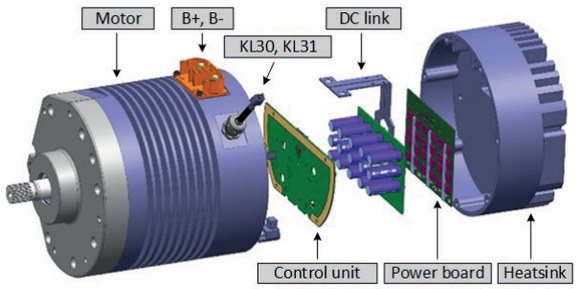

Figure 2: Exploded view of the EUT.

To accurately capture all EMI effects that are influenced by the rotation of the motor itself in the form of different current paths through the non-symmetrical geometry, a transient analysis must be performed, inevitably resulting in longer simulation times. A comparison between both approaches could be seen in the Table 1.

Table 1: Frequency vs. time domain.

Frequency domain	Time domain
(-) EMI receiver functionality (limited implementation)	(+) Complete EMI receiver functionality (IF filter, STFT, detectors, dwell time)
(-) Circuit analysis presumes stationary conditions	(+) Space Vector Pulse Width Modulation
(-) Complex non-linear SPICE models not possible to use	(+) Possibility to use official non-liner SPICE models (e.g., MOSFETs)
(+) Instant simulation results with high convergence	(-) Time consuming simulation with convergence issues

To mitigate long simulation time and convergence issues, a good understanding of the EM spectrum sensitivity to different parasitic components is beneficial. By that, to simplify the model and thus shorten the simulation time, we can exclude those with negligible effect to the spectrum.

3 Modelling

According to the Fig. 3, the LTspice® environment was used to construct an appropriate schematic for transient analysis. Signal post-processing, corresponding to the EMI receiver, was done using MATLAB®.

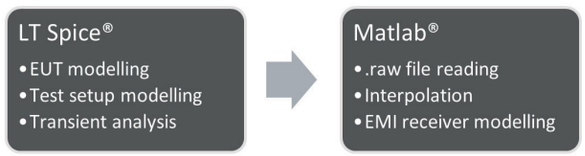

Figure 3: Modelling flow.

The EUT has a dedicated 12 V power supply line for the logic board, which is separate from the main 48 V battery power supply in terms of grounding. This setup enables us to observe and address conductive emissions for each part separately. In this paper, our focus will be solely on the 48 V power stage.

3.1 CISPR 25 test setup

The baseline for the test setup modelling is a reference ground plane with two grounded Artificial Networks (Ans), where the EUT's housing is also grounded with a copper braid (see Fig. 4). This configuration establishes a return path for common-mode (CM) emissions. The power supply lines were 40 cm long, and their inductances are a part of the path for differential mode noise. The mentioned inductances were calculated analytically based on their geometry according to CISPR 16-2-1 [18].

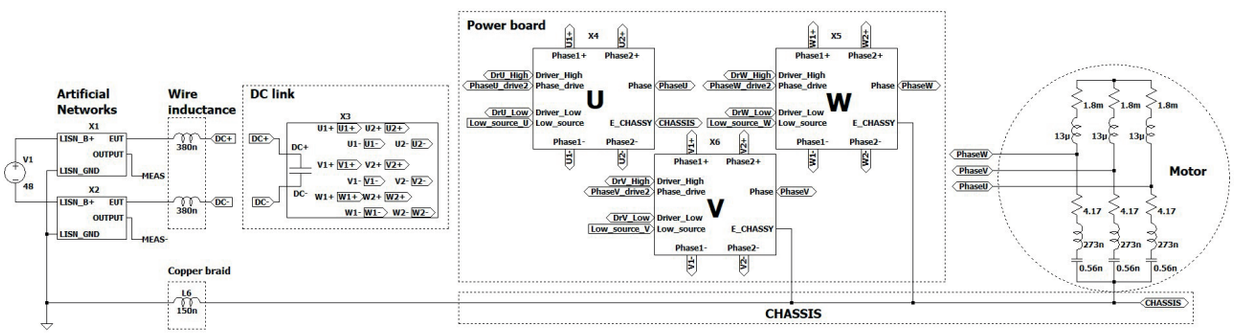

Figure 4: Top level EMI model including inverter (DC link, power board), motor and test setup according to CISPR 25.

$$L = 2l\left(\ln\frac{2l}{b+c}\right) + 0,5 + 0,22\frac{b+c}{l} \quad (1)$$

3.2 DC link

The DC link PCB assembly (PCBA) consists of four copper layers, as shown in the Fig. 5, with the internal two layers serving as DC positive and DC negative power planes. The two external layers contain multiple polygons to ensure a homogeneous load on each capacitor. This configuration forms a matrix of parasitic inductances that was modeled along with electrolytic and ceramic capacitors. Parasitic capacitances between the planes were neglected due to their small values in comparison to the capacitances of the capacitors.

The parasitic inductances, extracted with boundary element method (BEM), were recalculated into an average inductance per unit length (IPL) to establish a foundation for simplifying the matrix. This simplification results in fewer components and nodes for SPICE simulation.

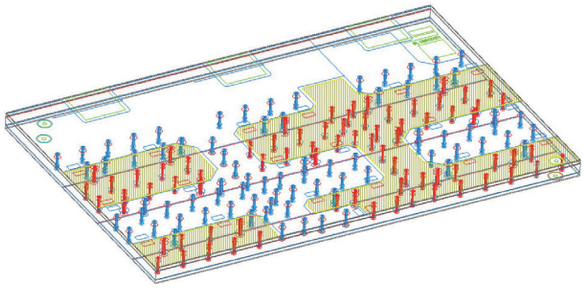

Figure 5: DC link PCB (Ansys® SIwave™).

The DC link matrix was modeled with 5 different horizontal inductances and 2 vertical ones. Each inductance has its own series resistance (see Table 2). The pads connecting the DC link to the power board are not symmetrically distributed, as shown in the Fig. 6.

Table 2: DC link parasitic parameters.

Parameter	Inductance [nH]	Series resistance [mΩ]
Lh1	0,88	0,22
Lh2	1,76	0,44
Lh3	2,4	0,6
Lh4	3,28	0,82
Lh5	1,4	0,35
Lv1	0,44	0,11
Lv2	1,64	0,41

3.3 Power board

The same approach to extract the parasitic elements from the Table 3 was used for the power board (see Fig. 7), where we sought the values of the parasitic inductances between the MOSFETs soldered onto the copper layer of the insulated metal substrate (IMS) [19].

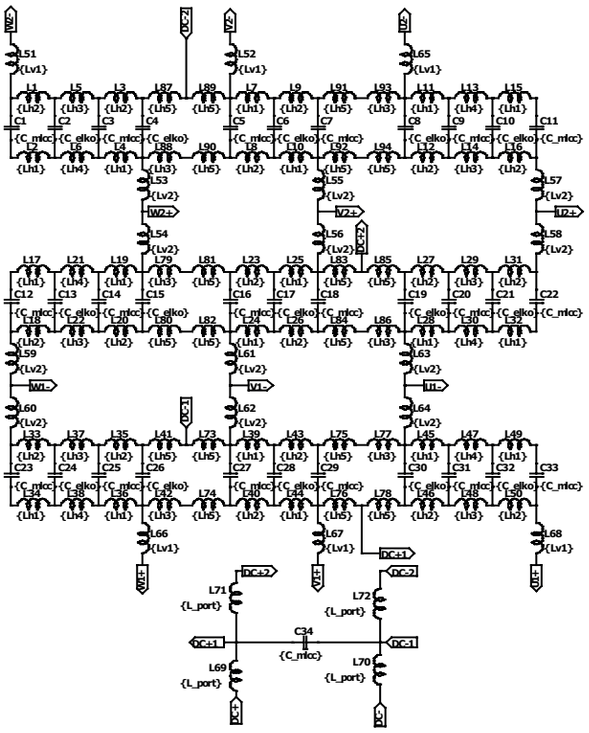

Figure 6: LTspice® model of the DC link.

Table 3: Power board PCB parasitic parameters.

Parameter	Inductance [nH]	Series resistance [mΩ]
L_pwr1	1,75	0,1
L_pwr2	3,5	0,2
L_phase	3,0	0,15

Parasitic capacitances of the polygons towards the substrate were calculated analytically. Capacitances of the B+ and B- polygons towards the substrate did not have an influence on the EMI spectrum due to the much higher capacitance of the Y-capacitors C1 and C2 from the Fig. 8. There was also a negligible influence of the parasitic inductances of the gate traces, whose values vary with the distance from the connector to the most distant MOSFET.

To model the MOSFET used in our experiment (Fig. 8), we applied the official SPICE model provided by the manufacturer. As the accurate switching element simulation is crucial for accurate EMI modelling, we verified the MOSEFET model adequacy by comparing the measured and simulated switching voltage transition shapes on a clamped inductive load according to Vrtovec et. al. [8]. Fig. 9 shows the setup for switching of the high side MOSFETs where the power board model is simplified for figure clarity.

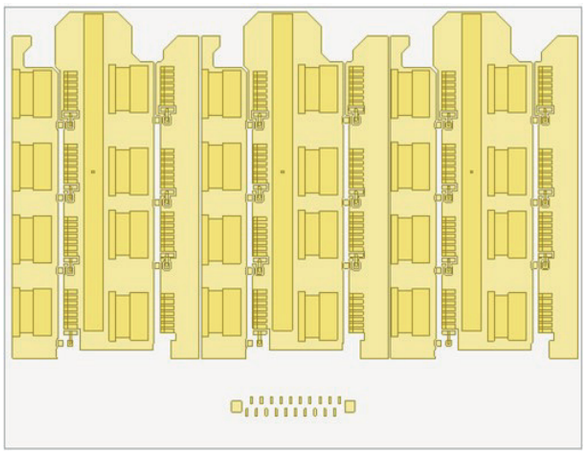

Figure 7: Power board PCB planes (Ansys® SIwave™).

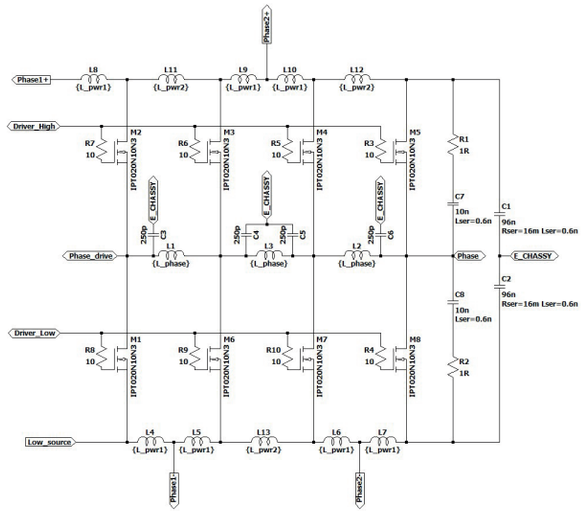

Figure 8: Power board single phase LTspice® model.

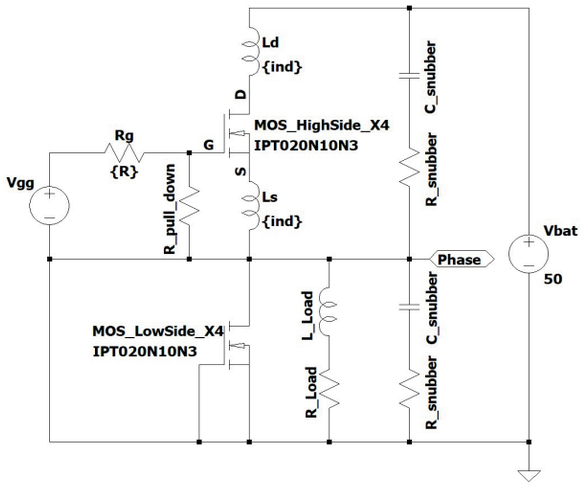

Figure 9: Test configuration featuring the clamped inductive load with V_{gg} controlling the high side MOSFETs. The measurements were taken using an inductive load of 40 µH and 6.66 Ω, achieving a current of 400 A_{DC} with the correct duty cycle, the V_{DC} was 50 V.

In the Fig. 10 we observe a good matching between the measured and simulated switching behavior of the high side MOSFETs (Phase V). It's crucial to note that the voltage-dependent capacitances of a MOSFET consistently influence the switching characteristics, alongside the inductances L_d and L_s originating from the PCB itself [8]. The latter is probably the cause for a slight phase shift between the graphs.

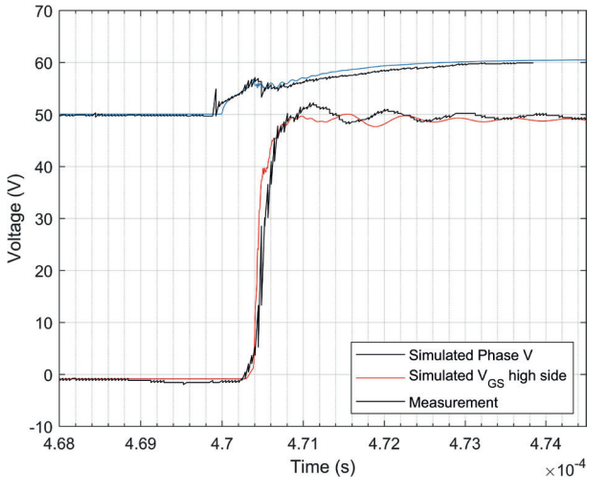

Figure 10: Switching sequence – high side ON. V_{GS} has an offset of +50 V for figure clarity.

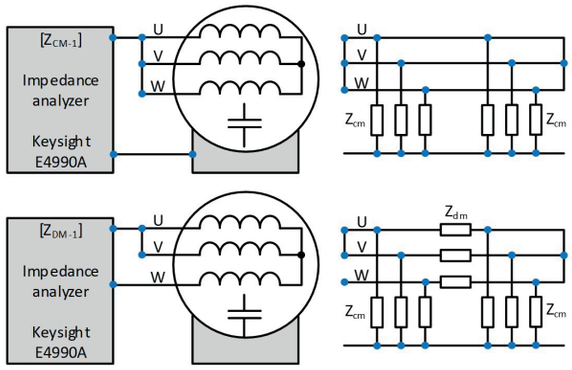

Figure 11: Common mode test configuration with motor equivalent impedance $Z_{CM\text{-}1}$ and differential mode test configuration with $Z_{DM\text{-}1}$ [13].

3.4 Motor

As already stated in the introduction, many researches propose an approach where lumped motor parameters are extracted through motor impedance measurements [10]–[15]. With this technique, a high-frequency model distinguishes common mode (CM) and differential mode (DM) impedances (see Fig. 11).

The $Z_{CM\text{-}1}$ measurement results in the Fig. 12 indicates a capacitive response in the low-frequency range, characterized by a single resonance point where inductance becomes predominant. It turns out that the

angular orientation of the rotor, representing the magnetic field of the permanent magnets with respect to the stator winding, exhibits minimal impact within the capacitive range of the $Z_{CM\text{-}1}$.

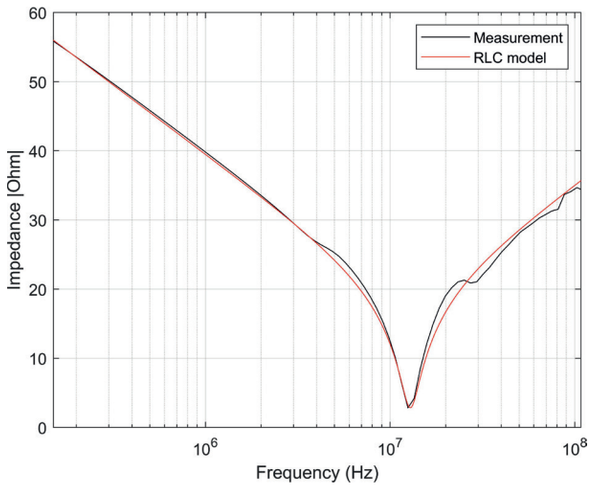

Figure 12: $Z_{CM\text{-}1}$ measurement results and approximation with RLC model.

From the high inductance of the windings, it also follows that the $Z_{DM\text{-}1}$ itself does not have a major influence on the *di/dt* produced during the switching sequence. Proceeding from this claim we can simplify the motor model where the $Z_{CM\text{-}1}$ represents CM propagation path and is independently combined with the winding characteristics.

To model the impedance behavior from the Fig. 12, we employed a simplified $Z_{CM\text{-}1}$ model with three basic RLC circuits, disregarding variations in rotor positions.

$$Z_{CM-1} = \frac{Z_{cm}}{3} \tag{2}$$

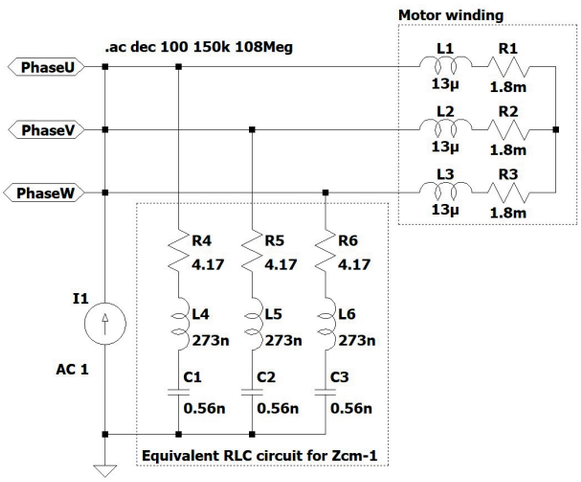

Figure 13: AC analysis model of the RLC circuit together with winding characteristics.

The proposed motor model from the Fig. 4 was evaluated with an AC analysis according to the Fig. 13 resulting in an adequate matching to the measured $Z_{CM\text{-}1}$ behavior (see Fig. 12).

4 EMI receiver

The characteristics of an EMI receiver must also be considered if we want to have an appropriate comparison between measured and simulated results of an EM spectrum. For historical reasons, the instrument characteristics are based on analogue super-heterodyne EMI receivers that sequentially scan frequency range of interest [20]. This approach is time-consuming and has been replaced with new digital Fast Fourier Transform (FFT) based instruments that comply with CISPR 16-1-1 [21], [22]. A basic block diagram of such a digital instrument can be found in the Fig. 14.

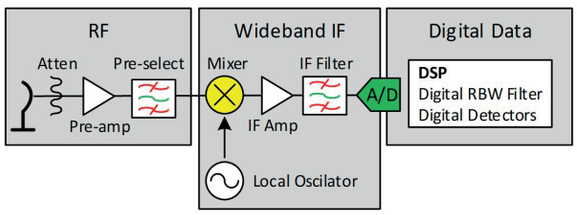

Figure 14: Block diagram of the FFT based EMI receiver [20].

4.1 MATLAB implementation of the EMI receiver

Within the SPICE transient simulation, the time step is varied according to the dynamics of the simulated results, thus an interpolation was performed to obtain a time vector with a constant time step. Generally, interpolation methods can introduce signal artifacts that could result in unrealistic spectral components. Thorough testing, we concluded that for the applied simulation conditions, the only method among the available within the MATLAB® environment that does not produce random overshoots between two simulated points was the Piece-wise Cubic Hermite Interpolating Polynomial (PCHIP) method.

CISPR 16 does not provide normative specifications for the parameters of the FFT. However, emerging from the Table 4, an appropriate windowing function must be used to meet the frequency response of the applied Intermediate Frequency (IF) filter, which originates from the superheterodyne principle [21]. Conventional EMI receivers generally apply a Gaussian window where the standard deviation of the windowing function is defined with the IF bandwidth for each frequency band. The windowing function also prevents spectral leakage caused by the discontinuity of the sampled signal.

Table 4: Bandwidth requirements for measuring receivers according to CISPR 16-1-1.

Frequency range [MHz]	f_{BW} [kHz]
0,15 – 30 (Band B)	9
30 – 1000 (Bands C & D)	120
1000 – 18000 (Band E)	1000

In the time domain, the Gaussian window function is transformed by the Short-Time Fourier Transform (STFT) into a Gaussian measurement bandwidth. This transformation results in discrete, overlapping measurement bandwidths in the frequency range. If a sine-wave carrier is positioned exactly between two measurement bandwidths, referred to as frequency bins, the result is a picket-fence effect (PFE) level error [20].

CISPR 16-1-1 requires accuracy better than ± 2 dB (± 2,5 dB above 1 GHz) for a sine-wave voltage measurement with 50 Ω resistive source impedance [21]. An overlap of more than 75% between the STFTs (see Fig. 15) ensures that the level measurement uncertainty for the pulse amplitude remains less than ± 1,5 dB [23]. In the used R&S ESR EMI test receiver, the STFT's overlap is at least 93%. The maximum level error is ± 0,4 dB, and the average level error just ± 0,1 dB [20].

Higher overlapping means longer computational time. To stay on the theoretical limit for the required error, an overlap of 75% was implemented, where *M* represents the number of applied windows (i.e., the number of STFT computations), including the measures for spectrum corrections [24]:

- dividing by the window length N_{win},
- multiplying by the factor of 2 to calculate single side spectrum,
- dividing by the factor of $\sqrt{2}$ to represent the measured power on 50 Ω input of the EMI receiver since the STFT algorithm returns the peak voltage value,
- dividing by the coherent amplification of the applied window G_C.

$$Gc = \frac{1}{N_{win}} \sum_{n=1}^{N_{win}} \left(w[n] \right) \tag{3}$$

STFT algorithm produces an array of complex numbers $\underline{X}(k,m)$, where the *k* th row corresponds to the amplitudes and phases of the frequency spectrum at frequency $K \cdot f_{res}$.

$$\underline{X}(k,m) = \frac{2}{\sqrt{2} N_{win} Gc} \sum_{n=1}^{N_{win}} \left(x\left[n + (m-1) N_{win} \left(1 - \frac{O_{proc}}{100} \right) \right] w[n] e^{-j 2\pi \frac{n\,k}{N_{win}}} \right) \tag{4}$$

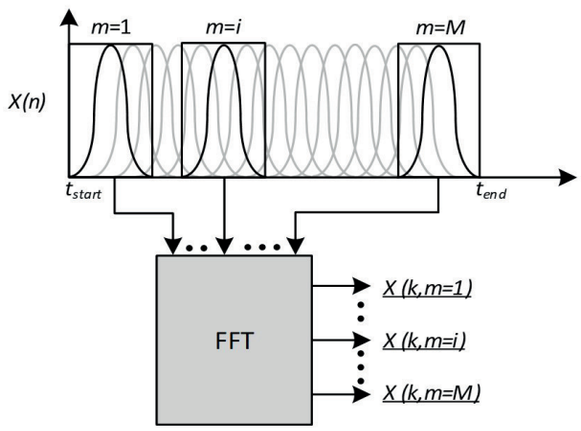

Figure 15: STFT overlapping.

By analyzing each individual row *m* of the complex array $\underline{X}(k,m)$ (see Fig. 16), it is possible to calculate the peak and average values at the observed frequency. The peak value is determined as the maximum value in the respective row.

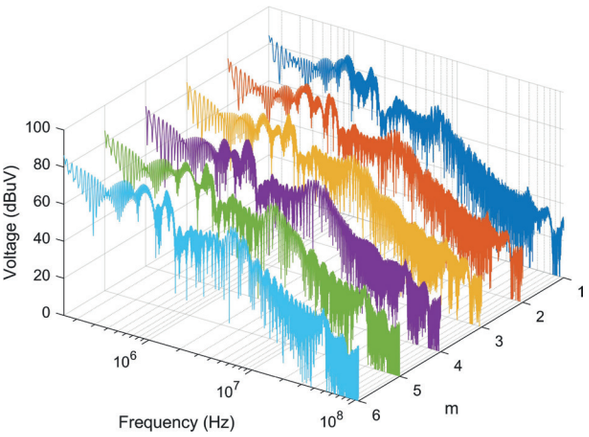

Figure 16: STFT algorithm without envelope detection.

$$X_{PK}(k) = \left| \underline{X}(k,m) \right|, m \in [1, M] \tag{5}$$

The average value for a certain *k* is calculated as the average of all absolute values in a certain row.

$$X_{AV}(k) = \frac{\sum_{m=1}^{M} \left| \underline{X}(k,m) \right|}{M} \tag{6}$$

5 Control strategy and results

The complexity of models, the number of nodes, and simulation parameters, have a direct impact on the duration of transient simulations and spectrum accuracy. The EUT employs the Space Vector Pulse Width Modulation (SVPWM) control strategy. To understand the influences of its implementation in the SPICE environment, we first implemented a simplified strategy where the PWM remains static.

5.1 Static PWM

The circuit from the Fig. 17 simulates a freeze-frame of a switching sequence, including dead-time. We analyzed EMI at 2 arbitrarily chosen static PWM switching sequences according to the Fig. 18, denoted by t_1 and t_2. The first PWM1 switching sequence from the Fig. 19

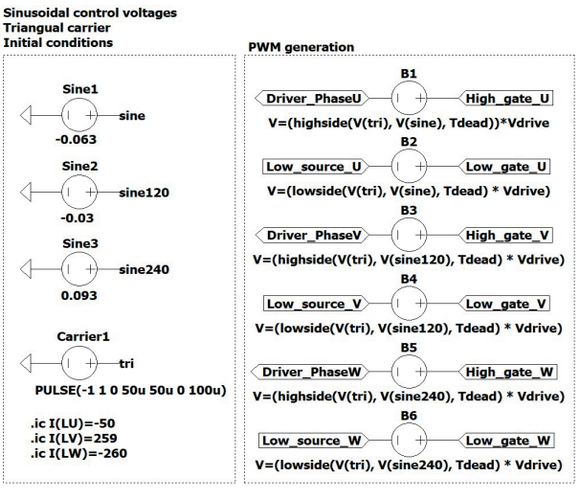

Figure 17: Static PWM1 implementation in LTspice®.

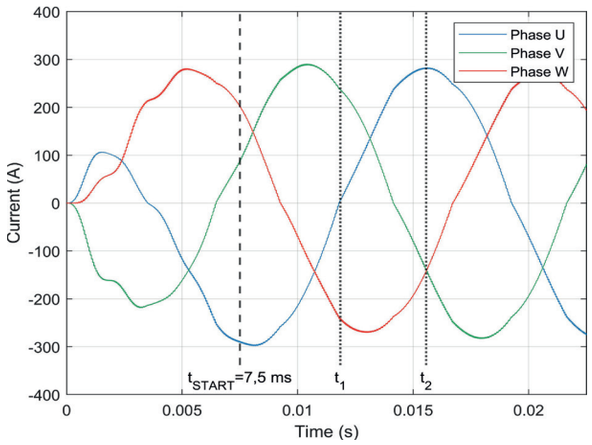

Figure 18: Simulated phase currents based on the SVPWM control strategy (t_{START} is the starting time for post-processing, t_1 and t_2 are times of the arbitrarily chosen static PWM switching sequences).

was set at t_1 when $I_{Phase\ U}$ goes through zero, while the second static PWM2 sequence was set at t_2 when $I_{Phase\ U}$ is at its peak value of 280 A.

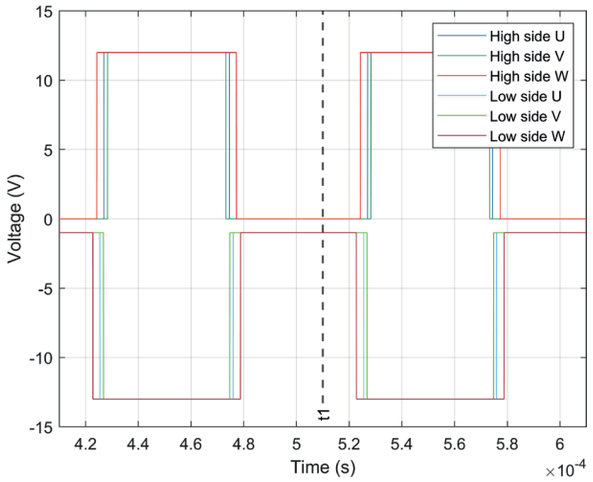

Figure 19: Static PWM1 switching sequence at t_1.

Here we show only the simulation setup at t_1 in detail, similarly was done for t_2. The switching frequency was 10 kHz, and the DC bus voltage was 48 V.

The approximation of this method lies in the inability to completely recreate PWM conditions at any SVPWM operating point. Therefore, it is important to set appropriate initial conditions to match the phase current values.

The input for the STFT algorithm cannot be infinitely short and must encompass at least a few overlapping windows to provide an adequate result. A time range of ± 0,5 ms around t_1 = 0,51 *ms* resulted in the application of six windows M = 6 (see Fig. 20).

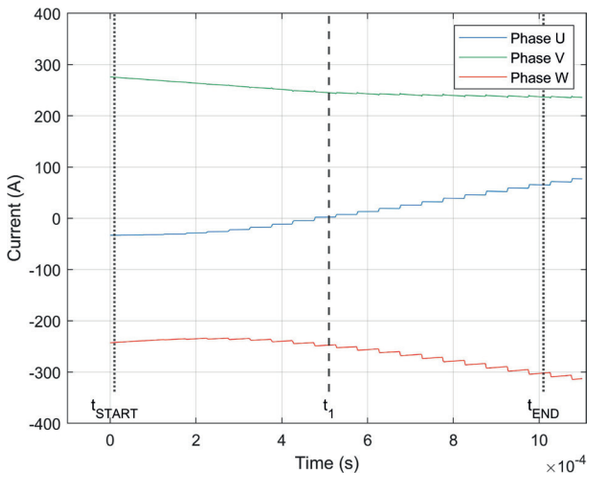

Figure 20: Simulated phase currents based on static PWM1 (± 0,5 ms around t_1 = 0,51 *ms*).

The simulated peak and average spectra for both sequences can be seen in the Fig. 21 and Fig. 22. The average spectral deviation for the switching sequence at t_1 is 7,34 dBµV and 3,79 dBµV, at t_2 is 6,35 dBµV and 3,65 dBµV for peak and average detectors, respectively. The transient analysis took 2 min to apply $M = 6$.

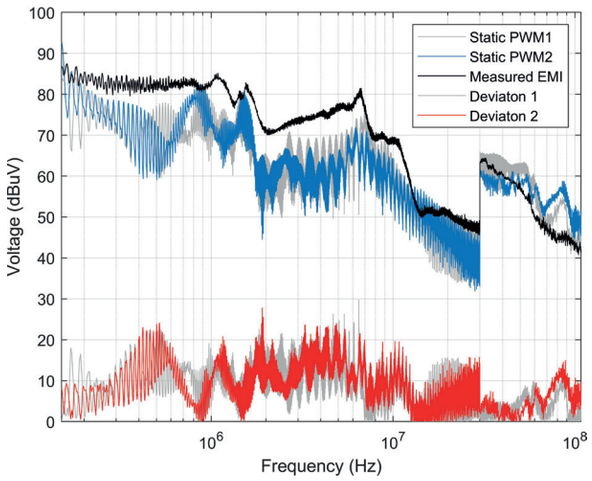

Figure 21: Comparison between measured and predicted peak detector spectrum (static PWM).

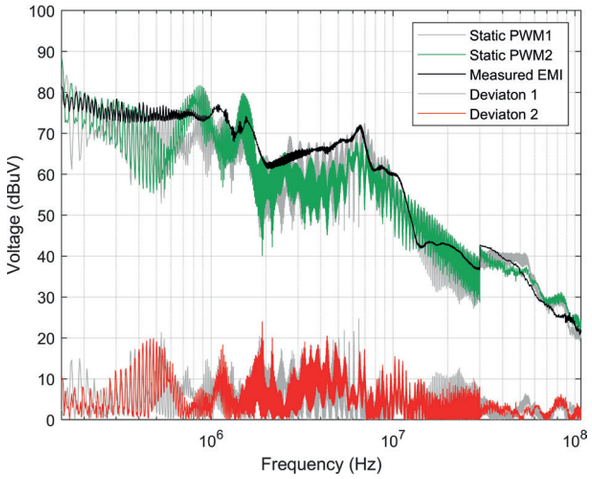

Figure 22: Comparison between measured and predicted average detector spectrum (static PWM).

5.2 Space Vector Pulse Width Modulation

To evaluate the effect of the motor rotation on the overall spectrum accuracy, the complete SVPWM control strategy for the inverter system was implemented in the LTspice® (see Fig. 23). The corresponding control strategy diagram is shown in the Fig. 24.

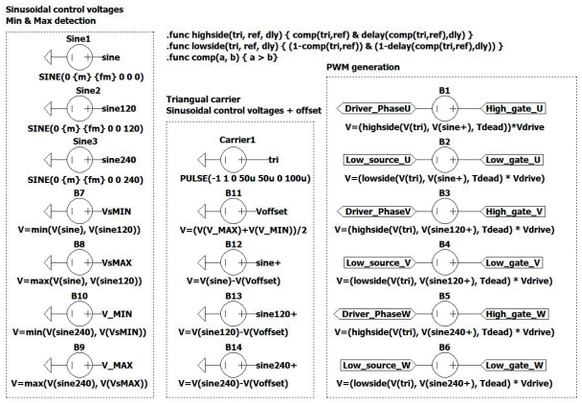

Figure 23: SVPWM implementation in the LTspice®.

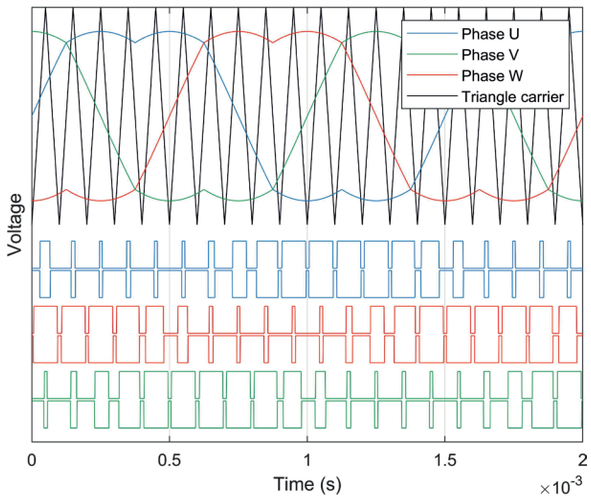

Figure 24: SVPWM control strategy (the chosen sequence is for figure clarity only and does not match the operating point at 1000 RPM).

The simulated peak phase current reached a value of 280 A_{PEAK} (200 A_{RMS}) by adjusting the appropriate modulation factor and other switching parameters according to the Table 5. On the EUT, the crossover distortion effect is mitigated within regulation algorithm.

Table 5: LTspice® switching parameters.

Parameter	Description
.param fm=66.6	Motor frequency
.param m=0.095	Modulation factor
.param Tdead=1.5e-6	Dead time

5.3 Transient analysis

The complexity of models, the number of nodes, and simulation parameters, have a direct impact on the duration of transient simulations. CISPR 25 requires operating the EUT under typical loading and other conditions

like those in a vehicle, ensuring that the maximum emission state occurs. The dwell time was 100 ms for 9 kHz and 10 ms for 120 kHz IF bandwidth, which must be appropriately translated into the simulation environment. To capture the entire spectrum of possible emissions produced by the motor drive, which in our case has 8 poles, we must set the simulation time to observe one electrical revolution of the motor at 1000 RPM.

$$t_{TRAN} > \frac{2\pi}{\frac{p}{2}\omega_m} = 15\,ms \tag{7}$$

As stated in the previous chapter, the LTspice® environment does not have the option to fix the time step due to convergence reasons, but it does have an option to limit its maximum value. In this case, the Nyquist theorem must be considered, with 108 MHz as the max frequency scale of interest.

$$f_{NYQUIST} < 2\,f_S = 2 \cdot 108\,MHz \tag{8}$$

$$t_{stepMAX} < \frac{1}{f_{NYQUIST}} \approx 4,63\,ns \tag{9}$$

In addition to the previously discussed minimum duration of the transient analysis (15 ms), we added 7.5 ms (total 22.5 ms) to ensure that all transient phenomena in LTspice® expired before t_{START}, including all phase currents reaching 280 A_{PEAK}, as it seen in the Fig. 18. The simulation setup was according to the Table 6.

Table 6: Simulation setup.

Parameter	Value
Processor, max. threads	Intel®Core™ i7-12700H, 20
Solver	Normal
Analysis	.tran 0 22.5m 7.5m 4.63n

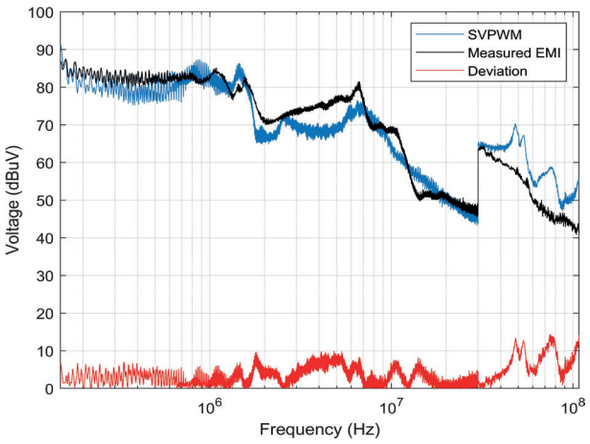

Figure 25: Comparison between measured and predicted peak detector spectrum (SVPWM).

The comparison of the measured and simulated EM spectrum for both detectors is shown in the Fig. 25 and Fig. 26, including the absolute deviation. The results show 3,33 dBµV and 2,58 dBµV of the average spectral deviation for peak and average detectors, respectively. The transient analysis took 43 min to capture one electrical revolution of the motor.

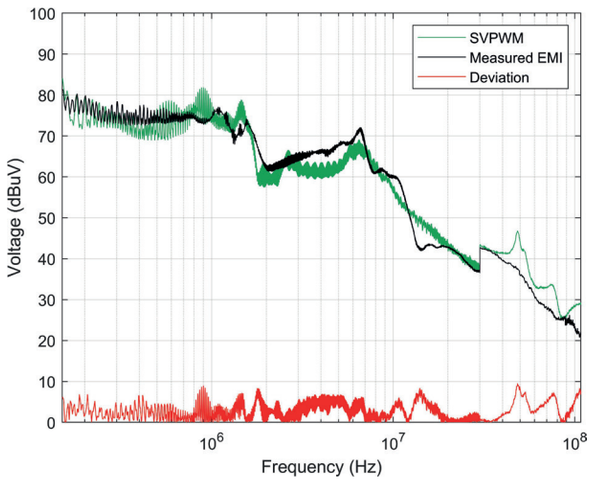

Figure 26: Comparison between measured and predicted average detector spectrum (SVPWM).

6 Conclusions

The proposed comprehensive strategy for modelling the conducted EMI of an integrated motor drive in the time domain was developed with the aim of finding a balance between overall simulation duration and spectrum accuracy.

For modelling the DC link and power board, we employed a direct approach to extract parasitic inductances between points of interest on the circuits, creating simplified matrices. This approach differed from using an automated Ansys® Q3D Extractor® feature, which generates a large matrix of lumped RLGC parameters. When extracting lumped motor parameters, we measured CM impedance through frequency sweep. Other parasitic elements were calculated analytically. This approach allowed us to maintain absolute control over the complexity of the matrices (i.e., to control the number of nodes and parasitic elements), directly addressing convergence issues and simulation duration in the LTspice® environment.

The implementation of the SVPWM control strategy improved the overall spectrum accuracy, considering the design of the EUT, with its large geometry resulting in different current paths during one electrical rotation of the motor. Neglecting this phenomenon leads

to the spectral value of a randomly chosen static PWM sequence deviating from the measured spectrum of a rotating motor. An additional improvement in the simulated spectrum was achieved with a proper EMI receiver implementation. The built-in response of the IF filters significantly impacted the spectrum, especially between multiple frequency ranges of the CISPR 16-1-1 standard.

An overview and comparison of the main factors of the SVPWM and static PWM methods can be seen in the Table 7.

Table 7: Comparison between static PWM and SVPWM simulation results.

Transient analysis	Static PWM1	Static PWM2	SVPWM
Simulation	2 min		43 min
.tran duration	1.01 ms		22.5 ms
Spectrum delta peak @150 kHz- 108 MHz	Average = 7,34 dBµV	Average = 6,35 dBµV	Average = 3,33 dBµV
Spectrum delta avg. @150 kHz- 108 MHz	Average = 3,79 dBµV	Average = 3,65 dBµV	Average = 2,58 dBµV

The proposed method with the SVPWM algorithm took 43 minutes to cover one electrical revolution of the motor, including the duration of the transient phenomena. Based on our experiences with developing multiple integrated motor drives, the resulting simulation time (i.e., < 1 hour) allows multiple iterations of model optimization without introducing bottlenecks in the development process. Simulation loops that take multiple hours or even days have limited repeatability, and their results are usually treated with low confidence since there is not enough time for parameterizing the parasitic elements to observe their impact on the spectrum.

The presented comprehensive strategy has a potential to be extended to other automotive products or even to other fields of interest where the accuracy of EMI prediction is highly dependent on changing current paths during the required dwell time.

7 Conflict of interest

The authors declare no conflict of interest.

8 References

1. B. Revol, J. Roudet, J. L. Schanen, and P. Loizelet, 'Fast EMI prediction method for three-phase inverter based on Laplace transforms', in *IEEE 34th Annual Conference on Power Electronics Specialist, 2003. PESC '03.*, 2003, vol. 3, pp. 1133–1138 vol.3, https://doi.org/10.1109/PESC.2003.1216608.
2. B. Revol, J. Roudet, J.-L. Schanen, and P. Loizelet, 'EMI Study of Three-Phase Inverter-Fed Motor Drives', *IEEE Trans. Ind. Appl.*, vol. 47, no. 1, pp. 223–231, Jan. 2011, https://doi.org/10.1109/TIA.2010.2091193.
3. E. Gubia, P. Sanchis, A. Ursua, J. Lopez, and L. Marroyo, 'Frequency domain model of conducted EMI in electrical drives', *IEEE Power Electron. Lett.*, vol. 3, no. 2, pp. 45–49, Jun. 2005, https://doi.org/10.1109/LPEL.2005.848730.
4. J.-L. Kotny and N. Idir, 'Time domain models of the EMI sources in the variable speed drives', in *2010 IEEE Energy Conversion Congress and Exposition*, 2010, pp. 1355–1360, https://doi.org/10.1109/ECCE.2010.5618276.
5. D. Zhuolin, Z. Dong, F. Tao, and W. Xuhui, 'Prediction of conducted EMI in three phase inverters by simulation method', in *2017 IEEE Transportation Electrification Conference and Expo, Asia-Pacific (ITEC Asia-Pacific)*, 2017, pp. 1–6, https://doi.org/10.1109/ITEC-AP.2017.8080876.
6. K. Wang, H. Lu, C. Chen, and Y. Xiong, 'Modeling of System-Level Conducted EMI of the High-Voltage Electric Drive System in Electric Vehicles', *IEEE Trans. Electromagn. Compat.*, vol. 64, no. 3, pp. 741–749, Jun. 2022, https://doi.org/10.1109/TEMC.2022.3147521.
7. A. Apelsmeier, C. Rettner, and M. Marz, 'Model for Conducted Emission of SiC Power Modules for automotive traction Inverter-Comparison to behaviour-based Model', in *2020 IEEE 21st Workshop on Control and Modeling for Power Electronics (COMPEL)*, Aalborg, Denmark, 2020, pp. 1–8, https://doi.org/10.1109/COMPEL49091.2020.9265805.
8. R. Vrtovec and J. Trontelj, 'Advanced gate control system for power MOSFET switching losses reduction with complete switching sequence control', *Inf. MIDEM*, vol. 46, no. 4, pp. 238–249, 2016, https://ojs.midem-drustvo.si/index.php/InfMIDEM/article/view/289.
9. Y. Kwack *et al.*, 'EMI modeling method of interior permanent magnet synchronous motor for hybrid electric vehicle drive system considering parasitic and dynamic parameters', in *2015 Asia-Pacific Symposium on Electromagnetic Compatibility (APEMC)*, 2015, pp. 78–81, https://doi.org/10.1109/APEMC.2015.7175390.

10. G. Vidmar and D. Miljavec, 'A Universal High-Frequency Three-Phase Electric-Motor Model Suitable for the Delta- and Star-Winding Connections', *IEEE Trans. Power Electron.*, vol. 30, no. 8, pp. 4365–4376, Aug. 2015, https://doi.org/10.1109/TPEL.2014.2352452.
11. F. Zare, 'Practical approach to model electric motors for electromagnetic interference and shaft voltage analysis', *IET Electr. Power Appl.*, vol. 4, no. 9, p. 727, 2010, https://doi.org/10.1049/iet-epa.2009.0305.
12. O. Magdun and A. Binder, 'High-Frequency Induction Machine Modeling for Common Mode Current and Bearing Voltage Calculation', *IEEE Trans. Ind. Appl.*, vol. 50, no. 3, pp. 1780–1790, May 2014, https://doi.org/10.1109/TIA.2013.2284301.
13. N. Idir, Y. Weens, M. Moreau, and J. J. Franchaud, 'High-Frequency Behavior Models of AC Motors', *IEEE Trans. Magn.*, vol. 45, no. 1, pp. 133–138, Jan. 2009, https://doi.org/10.1109/TMAG.2008.2006006.
14. A. Rahimi and K. Kanzi, 'High-frequency modelling of permanent magnet synchronous motor for conducted EMI studies', *IET Electr. Power Appl.*, vol. 14, no. 11, pp. 2027–2036, 2020, https://doi.org/10.1049/iet-epa.2019.0773.
15. S. Yang, L. Zhai, and G. Hu, 'Measurement-based Modeling of High Frequency Equivalent Circuit of Permanent Magnet Synchronous Motor of Electric Vehicle', in *2022 Asia-Pacific International Symposium on Electromagnetic Compatibility (APEMC)*, 2022, pp. 719–721, https://doi.org/10.1109/APEMC53576.2022.9888573.
16. 'CISPR 25: Vehicles, boats and internal combustion engines – Radio disturbance characteristics – Limits and methods of measurement for the protection of on-board receivers'. IEC, Geneva, 2016.
17. G. Ergaver and J. Trontelj, 'Prediction of Radiated Emissions of Automotive Electronics Early in the Design Phase based on Automotive Component Level Testing', *Inf. MIDEM*, vol. 46, no. 1, pp. 42–52, Mar. 2016, https://ojs.midem-drustvo.si/index.php/InfMIDEM/article/view/191.
18. 'CISPR 16: Specification for radio disturbance and immunity measuring apparatus and methods – Part 2-1: Methods of measurement of disturbances and immunity – Conducted disturbance measurements'. IEC, Geneva, 2017.
19. T. Skuber, 'Modeling and Optimization of Power Module for 48V High Power Inverter', *Inf. MIDEM*, vol. 51, no. 4, pp. 243–251, Dec. 2021, https://doi.org/10.33180/InfMIDEM2021.404.
20. B. Wangard, 'MIL-STD-461 Testing Advantages Using Time Domain Scan EMI Receivers'. Rohde & Schwarz, 2019, https://scdn.rohde-schwarz.com/ur/pws/dl_downloads/premiumdownloads/premium_dl_application/MIL-STD-461_Testing-Advantages-Using-Time-Domain-Scan-EMI-Receivers.pdf.
21. 'CISPR 16: Specification for radio disturbance and immunity measuring apparatus and methods – Part 1-1: Radio disturbance and immunity measuring apparatus – Measuring apparatus'. IEC, Geneva, 2015.
22. F. Krug and P. Russer, 'Signal processing methods for time domain EMI measurements', in *2003 IEEE International Symposium on Electromagnetic Compatibility, 2003. EMC '03.*, 2003, vol. 2, pp. 1289-1292 Vol.2, https://doi.org/10.1109/ICSMC2.2003.1429156.
23. S. Braun, A. Frech, and P. Russer, 'CISPR specification and measurement uncertainty of the time-domain EMI measurement system', in *2008 IEEE International Symposium on Electromagnetic Compatibility*, Detroit, MI, 2008, pp. 1–4, https://doi.org/10.1109/ISEMC.2008.4652078.
24. G. Ergaver, 'Raziskava elektromagnetnih sevalnih emisij elektronskih naprav za avtomobilsko področje', PhD diss., University of Ljubljana, Ljubljana, 2017, https://repozitorij.uni-lj.si/IzpisGradiva.php?lang=slv&id=92362.

Arrived: 03. 01. 2024
Accepted: 06. 02. 2024